A Smart, Responsive Crystalline Porous Organic Cage Membrane with Switchable Pore Apertures for Graded Molecular Sieving

Ai He[1,†], Zhiwei Jiang[2,†], Yue Wu[1], Hadeel Hussain[4], Jonathan Rawle[4], Michael E. Briggs[1], Marc A. Little[1], Andrew G. Livingston[2,3*], Andrew I. Cooper[1,5*]

[1] Department of Chemistry and Materials Innovation Factory, University of Liverpool, 51 Oxford Street, Liverpool L7 3NY, UK.

[2] Department of Chemical Engineering, Imperial College London, South Kensington, London SW7 2AZ, UK.

[3] School of Engineering and Materials Science, Queen Mary University of London, London E1 4NS, UK.

[4] Diamond Light Source, Didcot OX11 0DE, UK.

[5] Leverhulme Research Centre for Functional Materials Design, University of Liverpool, Liverpool L7 3NY, UK.

[†] These authors contributed equally to this work.

*Corresponding author. Email: a.livingston@imperial.ac.uk; aicooper@liverpool.ac.uk

Membranes with high selectivity offer an attractive route to molecular separations, where technologies such as distillation and chromatography are energy-intensive and tedious. However, it remains challenging to fine-tune the structure and porosity in membranes, particularly to separate molecules of similar size. Here, we report a process for producing composite membranes that comprise crystalline porous organic cage films fabricated by interfacial synthesis on a polyacrylonitrile support. These membranes exhibit ultrafast solvent permeance and high rejection of organic dyes with molecular weights over 600 g·mol⁻¹. The crystalline cage film is dynamic and its pore aperture can be switched in methanol to generate larger pores that provide increased methanol permeance and higher molecular weight cut-offs (1400 g·mol⁻¹). By varying the water/methanol ratio, the film can be switched between two phases that have different selectivities, such that a single, 'smart' crystalline membrane can perform graded molecular sieving. We exemplify this by separating three organic dyes in a single-stage, single-membrane process.

Porous organic cages (POCs)[1,2] are discrete molecules with intrinsic cavities that can create porosity in molecular crystals[1], amorphous solids[3], and porous liquids[4]. As a result of their shape-persistence, the adsorption properties of POCs can sometimes be predicted *in silico* from knowledge of their isolated molecular structures alone[5,6]. However, the adsorption properties of POC materials are also affected strongly by their solid-state packing[2,7]. For example, extrinsic pores in POC crystals can selectively adsorb guests, including rare gases[8], in addition to the intrinsic cavities in the cages themselves. Indeed, inefficient packing of POCs can generate solids with considerably more porosity than would be expected from the cage cavities alone[2,7]. It is this combination of intrinsic and extrinsic porosity that determines the functionality of POC-based materials in selective adsorption processes. This overall porosity fingerprint for POCs can be fine-tuned by controlling the cage packing; for example, to optimise their performance in molecular separations[9].

Most separation studies involving POCs have used molecular crystals[2,7], which can exhibit slow adsorption kinetics that might prohibit their larger-scale utilisation. Moreover, many approaches that use POC crystals rely on selective adsorption governed by thermodynamics, rather than kinetics, which limits their wider use in size and shape-selective membrane filters. Given their solution processability, however, there is scope to develop crystalline POC-based membranes that operate by selectively removing guests that are either too large or that have the wrong shape to diffuse through the POC pore structure.

There is growing interest in membrane technologies that perform industrial and environmentally relevant separations, particularly molecular separations in which two or more solutes are separated one from the other as in distillation or chromatography, as opposed to separations where a whole set of solutes is concentrated, as in evaporation or seawater reverse osmosis[10–14]. A key objective is to make these separations more sustainable and more efficient. A major advantage of membranes is that they can perform separations in the liquid phase, which is often more practically useful than vapors and also eliminates the need for phase changes.

Membranes for liquid separations are typically produced using phase inversion, which can be followed by coating[15] or interfacial polymerization[16]. A limitation of these synthetic processes is that they produce amorphous polymer networks with a modest degree of pore tunability. There is a strong demand to develop membranes with more tunable and modular pore structures. Various porous solids, including zeolites[17], POCs[1,2], organic polymers[18], metal-organic frameworks (MOFs)[19], covalent organic frameworks (COFs)[20], and hydrogen-bonded organic frameworks (HOFs)[21] have been explored as candidates to modify membrane separation behaviour. Banerjee *et al.* reported COF films with 1.4 to 2.6 nm pores that showed

good performance in dye rejection[22]. Dichtel *et al.* reported COF films with 3.4 nm pores and tunable thicknesses over the range of 100 μm to 2.5 nm that rejected up to 91% of an organic dye, Rhodamine WT, from water[23]. The same group also reduced the effective pore size of their COF membrane to 3.3 and 3.2 nm using reticular chemistry[24]. In addition to COFs[25,26], MOFs and their composites have been used to produce membranes[25,27]. However, despite these recent advances, it is still challenging to produce continuous nanofiltration membranes with extended porous frameworks that perform exclusively as size-based molecular sieves rather than selective adsorbents[28]. POCs have two distinct advantages over other porous crystalline solids: they are solution-processable and their solid-state structures are defined by non-covalent intermolecular interactions, which can be switched using chemical stimuli to alter their bulk porosity[29,30]. As such, POCs are intriguing but relatively unexplored candidates for new types of membrane materials[31–35]; indeed, many selectively porous POCs have been reported[36–39], and they offer the possibility of introducing tunable porosity or even smart, switchable porosity.

Many practically important molecular separations involve ternary systems or more complex mixtures—for example, separating multiple hydrocarbon fractions from light crude oil by distillation, pervaporation or organic solvent reverse osmosis[40,41]; purification of fatty acids[42,43], practically recovery of omega-3 polyunsaturated fatty acids from fish oil by nanofiltration[44]; or sieving out by-products from reactions, for example in the liquid phase peptide synthesis of pharmaceuticals[45]. To achieve equivalent separations for complex mixtures using membranes, cascades of membranes with graded molecular weight cut-offs have been developed[46], using phase inversion (polymeric membranes)[47] or sol-gel processing (ceramic membranes)[48] by manipulating the receipt of dope solution or fabrication conditions to produce multiple membranes with a variety of pore sizes. This places membranes at a disadvantage for ternary and higher separations—whereas a single distillation or chromatography column can produce multiple fractions with differing compositions. Separating more than binary solute systems using a membrane cascade requires multiple pumped recycle streams and complex fluid controls[49]. While solvent gradients are used with significant effect in chromatography to modulate solid-liquid interactions, there are as yet no reports of membranes that respond to solvent gradients by changing their solute selectivity.

Here, we report the fabrication of close-packed and defect-free films of a shape-persistent imine POC, **CC3,** which grow at the liquid-liquid interface between water and dichloromethane (Fig. 1a). The resulting material comprises highly crystalline domains of **CC3** in its most thermodynamically stable polymorph, **CC3**α (Fig. 1b). By coating the **CC3**α film on polyacrylonitrile (PAN), we produce a continuous membrane (**CC3**α-PAN) that has excellent permeance for both polar and non-polar solvents, including water (43.0 L·m^{-2}·h^{-1}·bar^{-1}) and

toluene ($55.9 \ L \cdot m^{-2} \cdot h^{-1} \cdot bar^{-1}$). Furthermore, we found that it is possible to rapidly and reversibly switch the membrane pore aperture using common solvents. Exposure of the non-covalent crystal packing of **CC3** in methanol (MeOH) induces a rapid phase transition from **CC3α** to a different crystalline phase, **CC3γ'**, which is less densely packed. This systematically increases the effective pore aperture of the resulting membrane, **CC3γ'-PAN** (Fig. 1c). This unique switching property of the **CC3γ-PAN** membrane allows the permeation of larger organic dyes that can be rejected in water while the large pore apertures are turned 'off' in the **CC3α-PAN** membrane. This switchable porosity is reversible, and surprisingly, it does not compromise the continuity of the membrane. This allowed us to separate three organic dyes with different sizes via graded sieving using a single membrane.
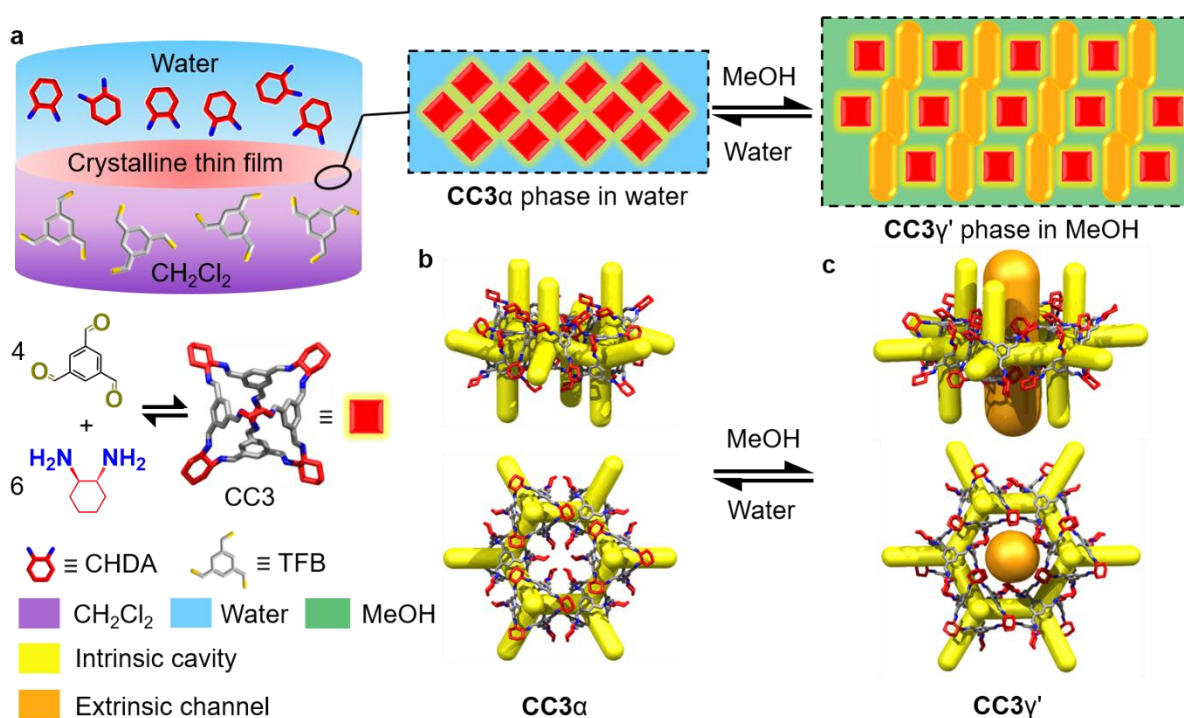

Figure 1 | Synthesis of a crystalline CC3 film and its crystal structures. a, Scheme showing the interfacial synthesis method used to fabricate crystalline **CC3** films, which were subsequently adhered to polyacrylonitrile (PAN) support. These crystalline cage films can cycle between two different forms, **CC3α-PAN** and **CC3γ'-PAN**, by cycling the solvent between water and MeOH. CHDA = 1*R*,2*R*-cyclohexanediamine; TFB = 1,3,5-triformylbenzene; CH_2Cl_2 = dichloromethane. **b**, **CC3α** structure with its 3D pore network shown in yellow. **c**, The **CC3γ'** structure, formed by soaking in MeOH, has additional extrinsic solvent-filled channels, shown here in orange, that opens up additional porosity in the membrane in response to the MeOH solvent.

Fabrication of Crystalline CC3 Films. Continuous films with highly crystalline domains of **CC3** were produced using a combined interfacial condensation reaction and crystallisation

process at a water-dichloromethane interface (Fig. 1a). This interfacial process allows the 2-component reaction of **CC3**, which is synthesized via a [4+6] cycloimination reaction using 1,3,5-triformylbenzene (TFB) and (1*R*,2*R*)-1,2-diaminecyclohexane (CHDA), while simultaneously directing the formation of **CC3** films at the interface (see Methods section and the Supplementary Information for experimental details). Continuous and freestanding **CC3** films were transferred from the liquid-liquid interface onto various substrates (*e.g.*, glass, steel mesh, carbon tape, and silicon wafers, Supplementary Fig. S1) for further analysis of the crystallinity and surface morphology. To perform permeance and dye rejection studies, the **CC3** film was coated onto a polyacrylonitrile (PAN) support by filtration to form the composite membrane (Fig. 2a). The resulting membrane, referred to hereafter as **CC3**-PAN, was free of macroscopic defects up to at least 7.4 cm in diameter using this preparation process (Supplementary Fig. S2), with no evidence of delamination after cutting the membrane into smaller pieces. The **CC3** film was characterised by Fourier transform infrared (FT-IR), Raman spectroscopy, nuclear magnetic resonance (NMR) spectroscopy, scanning electron microscopy (SEM), focused ion beam SEM (FIB-SEM), X-ray diffraction, and atomic force microscopy (AFM). For spectroscopic measurements, a crystalline **CC3**α sample was used as a reference[1]. **CC3**α has a 3D diamondoid pore structure and it is the thermodynamically most stable polymorph **CC3**[1]. The FT-IR spectrum of the **CC3** film showed the characteristic stretching band of the **CC3** imine bond at 1640 cm^{-1} (Supplementary Fig. S3). ^{1}H NMR spectroscopy was carried out after fully dissolving a **CC3** film in deuterated chloroform (CDCl$_3$) and this confirmed the formation of **CC3** but also showed a small amount (~2%) of unreacted aldehyde (Supplementary Fig. S4). Magnified optical images of the **CC3** film on a glass substrate suggested that the film was continuous (Supplementary Fig. S5). A Raman map was performed on an 80 × 80 µm^2 **CC3** film deposited on glass (Fig. 2b and 2c), which indicated that the **CC3** film comprised crystalline domains with the same solid-state structure as the **CC3**α polymorph (Fig. 2d and Supplementary Section 1.2 for full experimental details). SEM images showed a continuous, apparently defect-free film in the **CC3**-PAN composite (Fig. 2e and Supplementary Fig. S6a) with a thickness of ~80 nm measured on a freestanding film (Fig. 2f), which contained embedded, octahedral **CC3** crystals (Supplementary Fig. S7). Cross-sectional SEM images were obtained after step-by-step FIB trenching and polishing of both **CC3**-PAN (Supplementary Fig. S8) and a **CC3** film coated on a silicon wafer (Supplementary Fig. S9). The FIB-SEM images showed a clear boundary between the **CC3** film that is layered on top of the supports. To further investigate the film thickness, we performed AFM measurements after transferring the as-synthesised **CC3** film onto a silicon wafer. This again confirmed that the **CC3** film was continuous with a constant thickness of ~80 nm over a 10 µm distance (Fig. 2g, and 2h, Supplementary Figs. S6b, S8-9).

A key advantage of interfacial synthesis is that it can create continuous films of the product.[16,22] We used this here to direct the solution-processable **CC3** molecules and their crystals to assemble into continuous and densely packed membranes at the solvent interface. We also modified the reaction conditions to optimise the thickness, continuity, and crystallinity of the **CC3** film (Fig. 2h). This allowed us to create **CC3** films from the interfacial reaction that were four times thinner than the **CC3** film created by spin coating[40], which potentially allows for faster diffusion of liquids through the membrane. To further confirm the crystalline structure of the film, we performed a series of powder X-ray diffraction (PXRD) and grazing incidence X-ray diffraction (GIXRD) measurements on **CC3**-PAN (see Methods section). These diffraction measurements revealed that the **CC3** film was crystalline and had the same structure as **CC3α** (Supplementary Figs. S10-11).
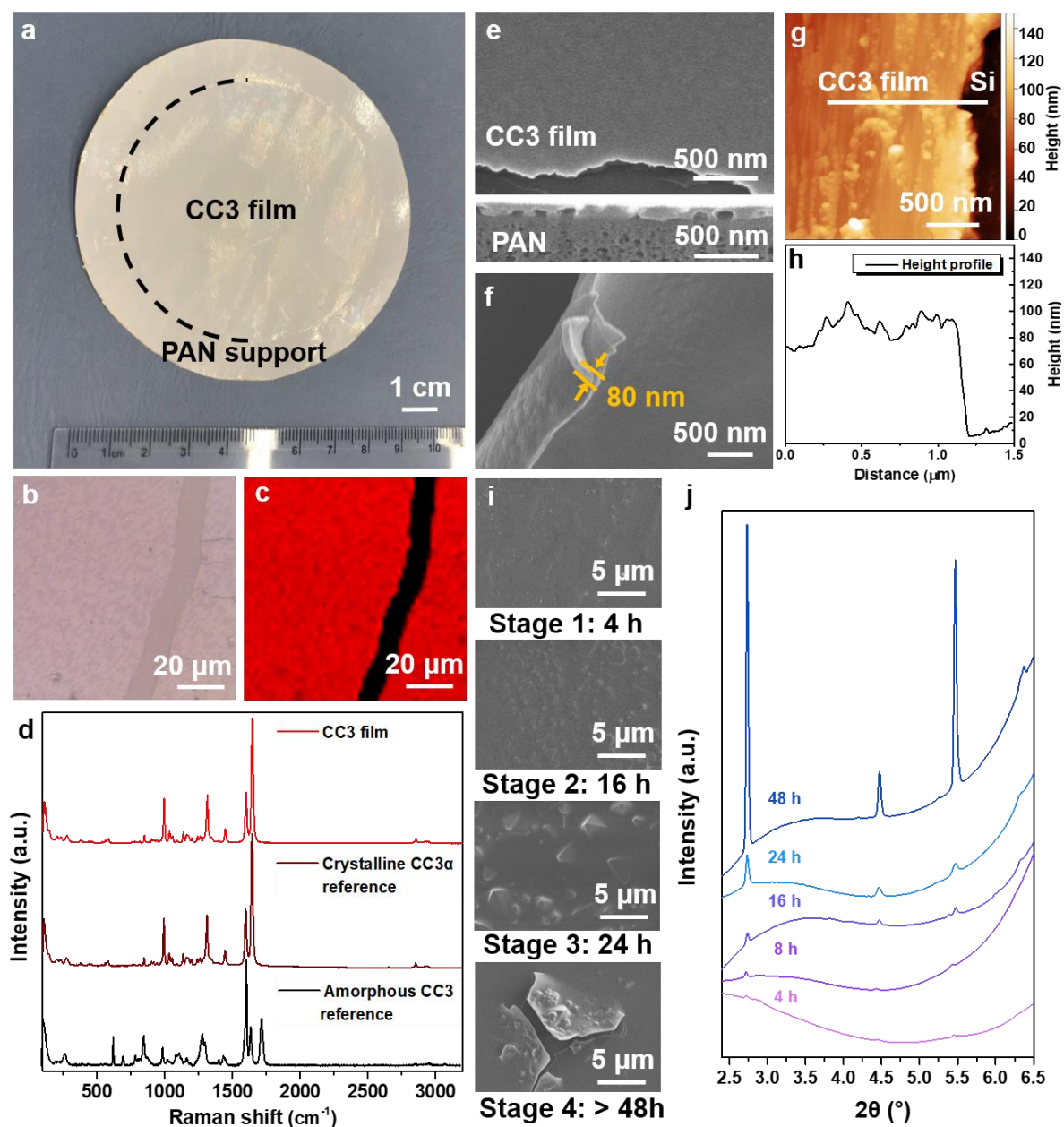
Figure 2 | Characterisation of a CC3α film. a, Photograph of a composite membrane **CC3α-PAN** with a diameter of 7.4 cm. **b**, Raman microscope image and **c,** Raman map of a **CC3α** film on a glass support, where we purposefully scratched the film before the measurement to expose the glass support (black stripe in **c**). The red regions on a **CC3α** film had comparable Raman spectra to a powdered crystalline **CC3α** reference[1]. **d**, Raman spectra of **CC3** film, **CC3α**, and amorphous **CC3**[3]. **e**, SEM image of **CC3α-PAN** showing the surface morphology of the **CC3α** film. Shown below is the cross-sectional FIB-SEM image of **CC3α-PAN**. **f**, SEM image of a freestanding **CC3α** film, where the film was deliberately buckled to show its thickness. **g**, AFM height image, and **h**, the height profile of **CC3α** film transferred onto a silicon (Si) wafer. **i**, SEM images of **CC3α-PAN-Xhr-0.8%** membranes formed at different reaction times, showing four stages of **CC3α** film formation. **j**, Out-of-plane GIXRD patterns of **CC3α-PAN-Xhr-0.8%** membranes fabricated using reaction times of between 4–48 hours.

To further investigate the crystallisation process of **CC3** films at the solvent interface, we varied the reaction time from 4 to 96 hours and manipulated the reagent concentrations from 0.2 to 2.5 wt.%. We use the nomenclature **CC3α-PAN-Xhr-Y%** to refer to the membranes made with X hours of reaction time and Y weight percent of the reagents. SEM, FIB-SEM, AFM, and Raman microscope images and maps revealed that thicker films with larger crystals were produced as the reaction time and reagent concentrations were increased (Supplementary Figs. S12-21). By contrast, using a reagent concentration of 0.2% resulted in poorly crystalline **CC3** membranes (Supplementary Figs. S14-15). For the reactions with reagent concentrations of 0.8%, the **CC3** film thickness increased with reaction time (30–600 nm from the 4–60 h reactions, see Supplementary Figs. S16-17). FIB-SEM images revealed there were triangle/octahedral shaped crystals embedded in the **CC3** films from the 32 and 48 h reactions (Supplementary Figs. S18-20); larger **CC3** crystals (1–10 μm) were observed on the substrate in the 72 and 96 h reactions (Supplementary Fig. S15-16). When the reagent concentration was increased to 2.0%, multiple **CC3** films were found stacked on top of one another (Supplementary Fig. S21). Based on these observations, we suggest that the interfacial synthesis occurs in four stages (Fig. 2i): Stage 1 (0–4 hours), interfacial polymerization of a continuous oligomeric film at the dichloromethane-water interface with no observation of **CC3α** crystals; Stage 2 (4–16 hours), self-sorting of the reactants and oligomers into the **CC3α** product and the formation of a partially-reacted, semi-cage film; Stage 3 (24–48 hours), crystallisation of **CC3α** and the formation of octahedral crystals in the film; Stage 4 (48–96 hours), formation of defects in the film, caused by larger octahedral crystals creating cracks and imperfections. GIXRD measurements demonstrated the crystallisation process across these stages, where the crystallinity increased with a longer reaction time (Fig. 2j). We, therefore, focused attention on the properties of **CC3α-PAN-24hr-0.8%**, referred to hereafter

as **CC3α**-PAN. This four-stage mechanism explains the differences that we observed in the permeance and selectivity of **CC3α**-PAN membranes produced using different reaction times and reagent concentrations, as discussed below.

Membrane Performance of CC3α-PAN. To determine the permeance and dye rejection performance of **CC3α**-PAN, we performed a series of filtration experiments in dead-end cells using solvents and dyes with different sizes and chemical functionalities (Supplementary Table S1, Figs. S22-23).

With a water contact angle of 94° (Supplementary Fig. S24), the **CC3α**-PAN membrane was stable in a range of polar and non-polar solvents (Supplementary Fig. S25), proving that these solvents do not dissolve **CC3**, and this led to ultrafast solvent permeances (Fig. 3a, see Supplementary Fig. S26 for blank PAN data). We attribute this to the 3D interconnected porosity through the **CC3α** crystals in the film. By comparison, an amorphous **CC3** membrane prepared by spin-coating (Supplementary Section 1.2) exhibited a 30 fold lower solvent permeance under the same testing conditions (Supplementary Fig. S27), although it should also be noted that the amorphous **CC3** membrane was four times thicker[31]. Apparently, the crystalline **CC3α**-PAN provides sufficient robustness to support the interconnected channels under high applied pressures. To further confirm the importance of crystallinity, **CC3α** membranes with different crystallinity levels were fabricated at each of the four reaction stages, simply by controlling the reaction time. A partially crystalline membrane (**CC3α**-PAN-8hr-0.8%) at Stage 2 exhibited a water permeance of 3.0 $L \cdot m^{-2} \cdot h^{-1} \cdot bar^{-1}$; that is, an order of magnitude lower than the fully crystalline Stage 3 membrane (49.5 $L \cdot m^{-2} \cdot h^{-1} \cdot bar^{-1}$ for **CC3α**-PAN-48hr-0.8%) prepared with prolonged reaction times (Fig. 3b). **CC3α**-PAN-8hr-0.8% and **CC3α**-PAN-48hr-0.8% both exhibited the same molecular weight cut-off (MWCO), as determined by filtering a range of dyes through the membranes (Fig. 3c). By comparison, amorphous oligomeric membranes produced in Stage 1 (**CC3α**-PAN-4hr-0.8%), and also cracked highly crystalline membranes produced in Stage 4 (**CC3α**-PAN-96hr-0.8%), exhibited unexpectedly higher water permeances but failed to achieve comparable separation performances, indicating that they contained physical defects.
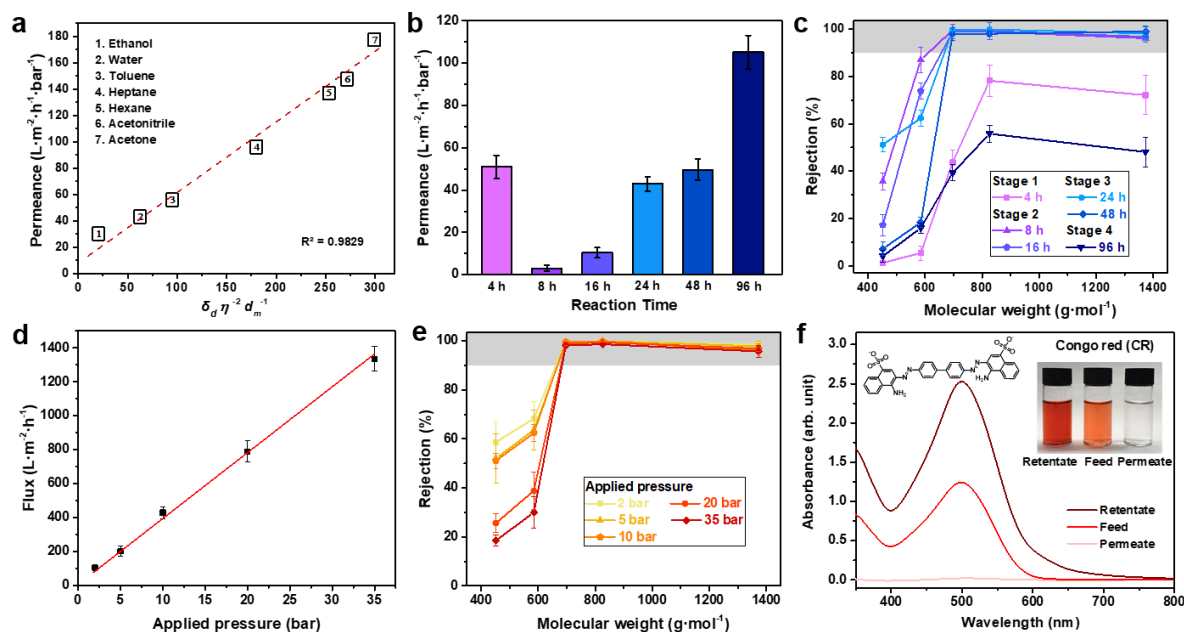
Figure 3 | Nanofiltration performance of CC3α membranes. a, Plot showing pure solvent permeances *versus* their combined solvent properties (viscosity η, molar diameter d_m, and solubility parameter δ_d) for **CC3α-PAN**, where R^2 is the coefficient of determination for the function. Hansen solubility parameter (δ) and the physical properties of each organic solvent are listed in Supplementary Table S2. **b,** Water permeance for **CC3α-PAN-Xhr-0.8%** membranes fabricated using reaction times that ranged between 4–96 hours. **c,** Dye rejection measurements for **CC3α-PAN-Xhr-0.8%** membranes in water. **d,** Water flux, and **e,** dye rejections of a **CC3α-PAN** membrane under a range of applied pressures. **f,** UV-vis absorption spectra of congo red (CR) in water before (feed) and after (permeate and retentate) selectivity tests performed with **CC3α-PAN**. Inserts show photographs of the feed, permeate, and retentate solutions, and the molecular structure of CR. Dye rejection was calculated using the intensity of the maximum absorption peak in the permeate and the feed and *Eq.* 3 in the Methods section. Mass balance calculations were performed using the maximum absorption peaks values of the feed, permeate, and retentate with *Eq.* 4. All error bars depict the standard deviations (*SD*) of the data points obtained from at least three independent membranes.

Two limitations of membranes produced from other crystalline porous materials, such as COFs, are poor stability at high pressures[22] and the interference of adsorption processes[28]. To explore these issues, the **CC3α-PAN** membrane was tested under a range of applied pressures, up to a maximum of 35 bar. The water flux increased linearly with increasing applied pressure (Fig. 3d), without affecting the MWCO (Fig. 3e). Longer duration studies demonstrated the mechanical robustness of **CC3α-PAN** and showed consistent dye rejection (99.7% for rose bengal) and water permeance (~43 L·m⁻²·h⁻¹·bar⁻¹) over 20 hours (Supplementary Fig. S28).

The applied pressure of 35 bar is an order of magnitude higher than used for liquid filtration through COF membranes[22], which suggests that these **CC3α**-PAN membranes might be more competitive for separations that require higher pressures.

To confirm that dye adsorption did not contribute to the selectivity performance of **CC3α**-PAN, mass balance calculations were used to measure the dye concentration in the retentate during the separations. After permeating 48 mL of Congo red (CR) feed, the absorption intensity of CR in the retentate increased from 1.24 to 2.53, while its absorption intensity in the permeate was only 0.02. In combination, these values are consistent with ~100% of the dye being rejected (Fig. 3f and Supplementary Figs. S29-30). These measurements also correlate with the observation of a colorless membrane surface after the dye filtration experiments (Supplementary Fig. S2). To further illustrate this, soaking powdered crystals of **CC3α** (100 mg) into aqueous solutions containing 20 ppm of the dyes (100 mL), led to no adsorption in the crystals after 7 days (Supplementary Fig. S31). These results all indicate that the dyes were rejected by the membrane, rather than being adsorbed.

Switchable Pore Aperture for Graded Sieving. Previous studies have shown that certain POCs can be switched between more than one polymorph to modify the porosity in the materials[29,30]. The solid-state structure of **CC3** has been directed into different polymorphs by crystallization from specific solvents[50], but until now, the solid-state transformation of **CC3** crystals was not explored. We were motivated to investigate whether a solvent stimulus could be used to switch the solid-state structure of the **CC3α** membrane film, thus changing the pore apertures and affecting the separation behavior.
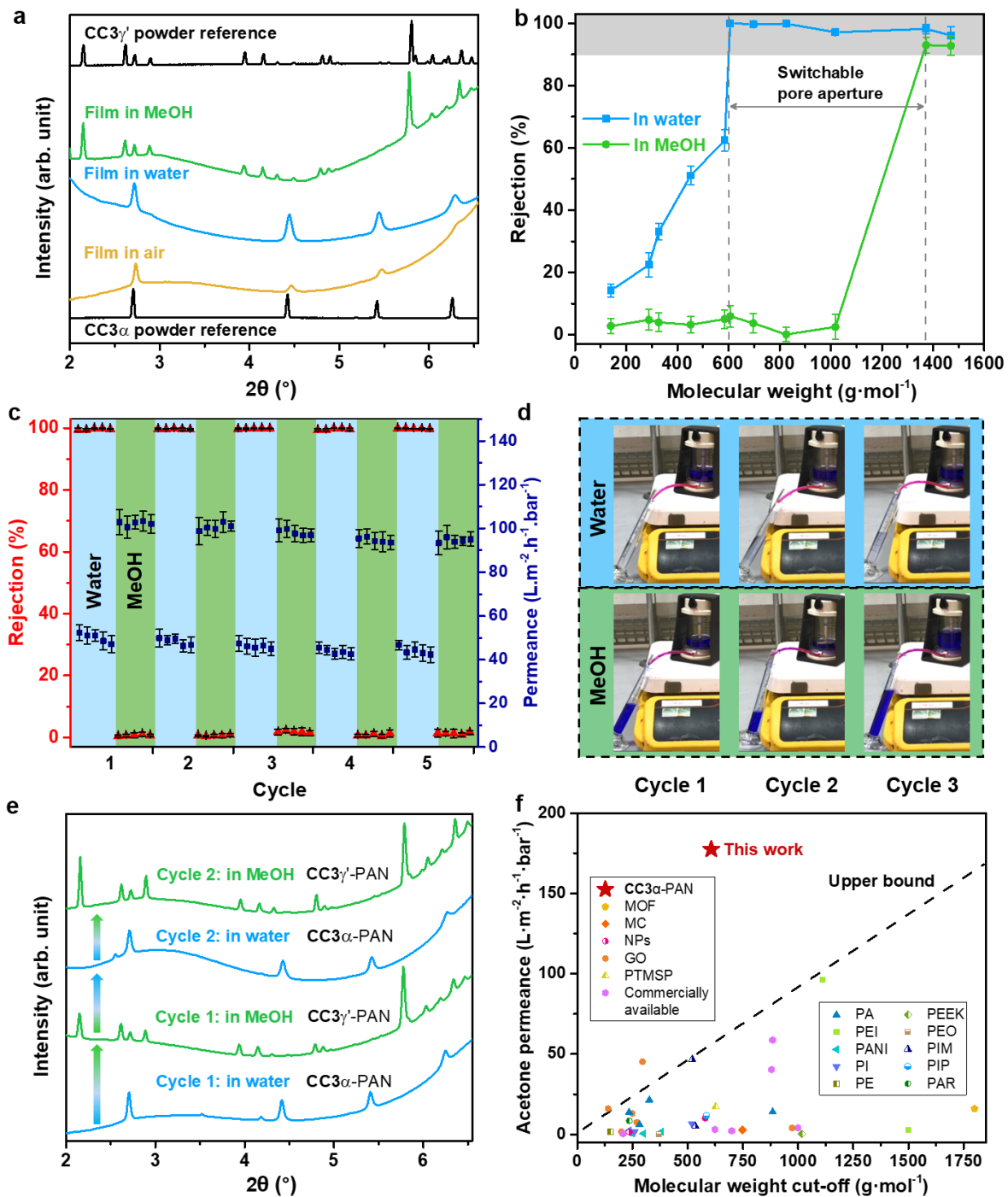
Figure 4 | X-ray diffraction characterisation and switchable separation performance of CC3-PAN membranes. a, GIXRD patterns confirm the structure of **CC3α**-PAN in air and water, and **CC3γ'**-PAN in MeOH. Experimental PXRD patterns of **CC3α** and **CC3γ'** powders are included as references. **b**, MWCO curve for **CC3α**-PAN in water and **CC3γ'**-PAN in MeOH containing 20 ppm dye solutes. The MWCO was determined by interpolating from the plot of rejection against the molecular weight of the dyes and corresponds to the molecular weight for which rejection reaches 90%. All error bars depict the *SD* of the data points obtained from at least three independent membranes. **c**, Reversible dye rejection of brilliant blue (BB) and

solvent permeance of the **CC3**-PAN membrane observed upon switching the feedstock solvent between water and MeOH. All error bars denote the standard deviations (*SD*) for measurements from at least three independent membranes. **d**, Photographs of a **CC3**-PAN in a filtration dead-end cell captured from Supplementary Video S1 at different filtration times; BB is rejected in water by **CC3α**-PAN while **CC3γ'**-PAN does not reject BB in MeOH. **e**, *In situ* GIXRD patterns showing the reversible phase transition of the cage membranes between **CC3α**-PAN and **CC3γ'**-PAN, switched by cycling 100 mL solvent between water and MeOH. **f**, Acetone permeance versus MWCO of generally solutes in acetone for nanofiltration membranes reported in the literature and **CC3α**-PAN. MOF, metal-organic framework; MC, macrocycle; NPs, nanoparticles; GO, graphene oxide; PTMSP, poly[1-(trimethylsilyl)-1-propyne]; PA, polyamide; PEI, polyethyleneimine; PANI, polyaniline; PI, polyimide; PE, polyethylene; PEEK, Poly(ether ether ketone); PEO, poly(ethylene oxide); PIM, polymers of intrinsic microporosity; PIP, piperazine; PAR, polyacrylate (see Supplementary Table S9 for further details).

We found that both air-dried and water-solvated films exhibited the same diffraction patterns as the reference peaks of **CC3α** powders measured by PXRD (Fig. 4a). A series of GIXRD patterns were then recorded after submerging the membrane in various organic solvents. Solvating in acetone and acetonitrile caused small shifts in diffraction peak positions due to solvent swelling, without significant structural changes to the **CC3α** phase (Supplementary Figs. S32-33). By contrast, the crystalline **CC3α** film transformed into a new structure when submerged in MeOH (Fig. 4a). By indexing the GIXRD pattern, we confirmed this was a MeOH-solvated **CC3** phase (**CC3γ'**, Supplementary Fig. S34) that was isolated previously by crystallising **CC3** from dichloromethane and MeOH[51]. The **CC3γ'** structure has monoclinic *C*2 crystal symmetry and its crystal packing is very different from **CC3α**. In its thermodynamically most stable polymorph, **CC3α**[52], the cage packs in a window-to-window arrangement to generate an interconnected diamondoid pore network (yellow channels in Fig. 1b). By contrast, in the **CC3γ'** phase, the **CC3** molecules are packed in a less dense arrangement, thus providing large extrinsic pores between hexagonally arranged **CC3** molecules (orange channels in Fig. 1c).

To investigate the structural transformation between **CC3α**-PAN and **CC3γ'**-PAN, we performed a series of in-situ GIXRD measurements while dosing the membrane surface with solvent vapour and after coating the membrane surface in a thin solvent layer (see Methods section and Supplementary Information for full experimental details). **CC3γ'**-PAN formed by immersion in MeOH transformed back into **CC3α**-PAN after being immersed in water (Fig. 4e), with clear evidence of both phases found when the membrane was immersed in a mixture of water and MeOH, or if a small amount of MeOH remained in the sample (Supplementary Fig.

S35); or when the MeOH vapour evaporated from the membrane at room temperature (Supplementary Fig. S36). This was also confirmed by desolvating the crystals using variable temperature high-resolution PXRD measurement, where a bulk powdered sample of the **CC3γ'** suspended in MeOH in a capillary was gradationally heated (Supplementary Fig. S37).

We next used MeOH rather than water to dissolve the dyes and filtered these solutions through the **CC3**-PAN membrane under the same conditions. Interestingly, the MWCO shifted from 600 g·mol^{-1} in water to 1400 g·mol^{-1} in MeOH for the same membrane (Fig. 4b and Supplementary Figs. S38-39). By contrast, a commercial Synder® NDX nanofiltration membrane with a comparable MWCO (500–700 g·mol^{-1}) exhibited similar rejection behaviour in both water and MeOH (Supplementary Figs. S40-41). We attribute this dramatic change in MWCO to the phase transformation to **CC3γ'**-PAN in MeOH. We further investigated how crystallinity influences the switchable pore aperture by measuring dye rejection of **CC3**-PAN membranes that had lower crystallinity (fabricated using lower concentrations or shorter reaction times, Supplementary Figs. S42-S45). **CC3**-PAN-4hr-0.8% rejected 78.2% of brilliant blue (BB) from water compared to 52.7% from MeOH, while the less crystalline **CC3**-PAN-4hr-0.2% had a less distinct BB rejection performance (68.6% from water *vs.* 52.8% from MeOH). This reveals that the high crystallinity in the **CC3** membrane is essential for regulating its separation performance after switching its pore aperture using a solvent stimulus; more amorphous POC membranes behave similarly to amorphous polymers, such as Synder® NDX.

To perform switchable molecular separations while cycling between **CC3α**-PAN and **CC3γ'**-PAN, a single membrane was used interchangeably with water and MeOH feedstocks containing the BB dye for five consecutive cycles. We found that both water and MeOH permeances remained high after cycling between **CC3α**-PAN and **CC3γ'**-PAN (Fig. 4c, Supplementary Tables S5-S7, and Video S1). More importantly, the rejection of BB switches between ~100% in water to ~0% in MeOH in each cycle (Figs. 4c and 4d); that is, the membrane can be switched 'on' and 'off' using a solvent. This switchable membrane performance results from the reversible transition between **CC3α**-PAN and **CC3γ'**-PAN, which appears to be complete within the one minute that it takes to switch the feedstock (Supplementary Video S1), and creates alternative diffusion pathways through the membrane structure. We measured *in situ* GIXRD measurements on solvated **CC3** films while performing two consecutive cycles; we found that the composite membrane transformed cleanly between **CC3α**-PAN and **CC3γ'**-PAN when the solvent was switched between water and MeOH and back again (Fig. 4e). We attributed this switching phenomenon solely to the phase transition of **CC3** films, rather than swelling of the membranes. To validate this, the **CC3**-PAN membrane was soaked in acetone and acetonitrile for nanofiltration tests and was found to exhibit comparable MWCOs to those observed in water (Supplementary Figs. S41, S46) because the

same phase, **CC3α-PAN**, is present in these solvents (Supplementary Figs. S32-33). Remarkably, the acetone permeance of **CC3α-PAN** reached 177 $L \cdot m^{-2} \cdot h^{-1} \cdot bar^{-1}$ with a MWCO of ~600 $g \cdot mol^{-1}$, which is well above the upper bound performance for nanofiltration membranes reported in the literature (Fig. 4f, Supplementary Fig. S47, and Table S9, see citations for the relevant studies in Supplementary Information).
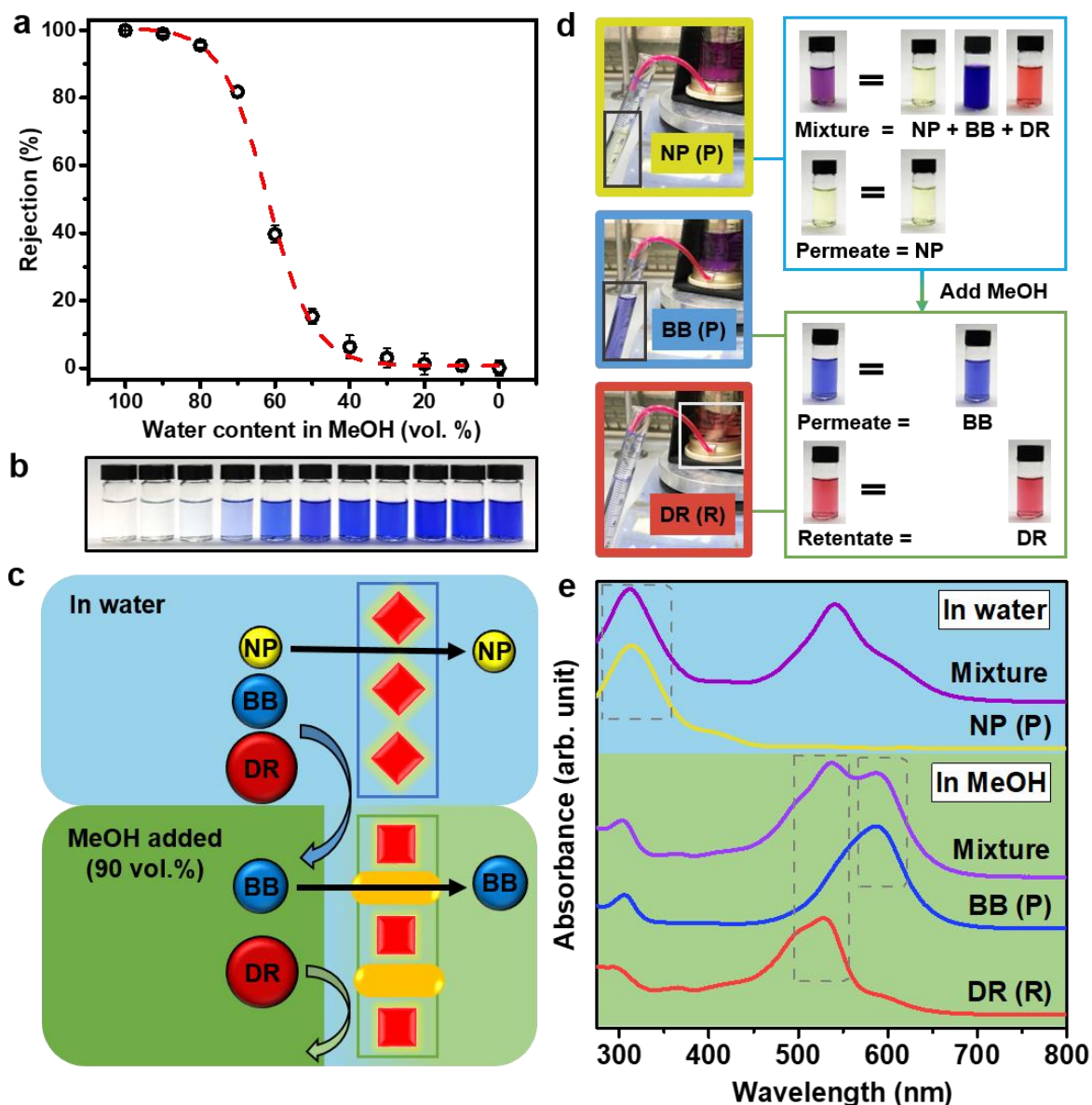
Figure 5 | Mixture fitting and graded sieving using a single switchable membrane. a, BB rejection in mixtures of water and MeOH (vol/vol) for **CC3**-PAN. All error bars depict the *SD* of the data points obtained from at least three independent membranes. The red dash line was fitted as the logistic function ($y = 1/(1 + \exp(-16.1 * (x - 0.617)))$), see Supplementary Section 1.4 for fitting method. **b,** Photograph of each permeate of BB in water and MeOH mixture with the water content ranging from 0–100 vol.%. **c**. Scheme showing ternary molecular separation

of three dyes direct red 80 (DR), BB, and 4-nitrophenol (NP) using one single membrane (**CC3**-PAN) in a continuous process: Step 1, **CC3α**-PAN in water only allows permeation of NP, leaving BB and DR in the retentate. Step 2, 90 vol.% MeOH was added into the retentate to transform the membrane structure to **CC3γ'**-PAN that only allows permeation of BB, leaving DR in the retentate. Liquid flushing was carried out between the steps to enrich the dyes in the retentate. **d**, Photographs showing the ternary molecular separation in a filtration dead-end cell, the nascent mixture feedstock, the permeate (P) collected in the first and second step, and the retentate (R) collected in the second step. **e**, UV-vis absorption spectra of the mixture containing three molecules in water, permeate from water, mixture and permeate from 90 vol.% of MeOH in water, and the remaining retentate. Note, the maximum absorbance wavelength for BB is 551 nm in water and 587 nm in MeOH; BB also shows absorbance at 305 nm in MeOH while NP shows its maximum absorbance at 312 nm in the same solvent.

A series of water and MeOH feedstocks containing the dye BB were used to determine the dynamic transformation between **CC3α**-PAN and **CC3γ'**-PAN. The critical transition between **CC3α**-PAN and **CC3γ'**-PAN occurred at a water concentration of 61.7 vol.% (Fig. 5a), after which a good rejection of BB was achieved (Fig. 5b). Understanding this dynamic transformation enables the manipulation of the pore aperture in a single **CC3**-PAN membrane by simply adjusting the water concentration in a water-MeOH mixture, without any activation processes[53] or the use of multiple membranes[22]. To demonstrate the potential advantage of this technology, we performed a graded sieving experiment to separate molecules from a ternary mixture using a single membrane. Initially, a water feedstock containing a mixture of three dyes, 4-nitrophenol (NP) (yellow, 139 g·mol⁻¹), BB (blue, 826 g·mol⁻¹), and direct red 80 (DR) (red, 1373 g·mol⁻¹) was filtered through the **CC3**-PAN membrane (Fig. 5c). Since **CC3**-PAN adopts its **CC3α**-PAN structure in water, the narrower pore aperture only allowed the smallest molecule, NP, to diffuse through the membrane, while the larger molecules, BB and DR were rejected and retained in the cell. Excess water was added into the cell to flush the residual NP from the retentate, and this process was repeated until the NP concentration in the permeate was below 1%. Subsequently, 90 vol.% of MeOH was added into the water retentate to generate a feedstock that transformed the membrane structure to **CC3γ'**-PAN with the larger pore aperture. BB could then diffuse through the membrane alone, while DR was retained in the cell (Fig. 5d, 5e). Finally, excess MeOH was used to flush any residue BB from the cell to leave only DR in the retentate, where it could be collected in pure form (see Supplementary Section 1.4 for full experimental details). As a result, by introducing a solvent gradient, a single membrane with a switchable pore aperture enables a ternary separation in a continuous process.

Conclusion and Outlook

We have developed a novel synthetic strategy to fabricate crystalline POC membranes using a coupled aqueous–organic interfacial reaction and crystallisation process. The continuous and defect-free POC membranes have achieved high permeances for a range of organic solvents—in some cases, such as for acetone, exceeding the upper performance bound—while also showing excellent separation performances. We have demonstrated the highly ordered crystalline structure of these POC membranes, with a switchable phase transition between two unique crystalline forms, **CC3α-PAN** and **CC3γ'-PAN**. This allows graded sieving to separate a mixture of three organic dyes using a single smart membrane and creates a membrane-based parallel to the widespread and highly effective use of solvent gradients in chromatography[54]. Besides, these POC membranes with switchable pore apertures could lead to new applications in triggered drug delivery[55], biosensors[56], or fermentation/fractionation processes[57].

While the current synthesis process makes it challenging to implement these POC membranes in commercial processes, it is conceivable that a more scalable production method might be developed in the future; for example, by exploiting the solution processability of these molecular cages. Future efforts will focus on using computational methods, such as crystal structure prediction (CSP), to design POC crystals with specific properties that can be designed from first principles.

Methods

Interfacial Synthesis of Crystalline CC3 Films. An aqueous solution of CHDA (0.26 g, 2.24 mmol, 0.8 wt.%) in water (32 mL) was carefully layered on top of a dichloromethane solution (30 mL) that contained TFB (0.24 g, 1.48 mmol, 0.8 wt.%) and was stored in a glass dish with an inner diameter of 7.4 cm (Fig. 1a). The interfacial reaction was covered and kept at room

temperature (~19-21 °C) for between 4–96 hours (typically, 24 hours). The continuous crystalline **CC3** film that grew at the dichloromethane-water interface was then isolated as a freestanding film that could then be layered directly onto different substrates, including glass, steel mesh, carbon tape, and silicon wafers. To perform liquid permeation studies, the **CC3** film was transferred onto PAN support to form composite **CC3**-PAN membranes, which were then soaked in pure water for 1 day. See Supplementary Section 1.2 for full experimental details and the reaction setup in Supplementary Fig. S48. Fabrication of PAN supports via phase inversion is presented in Supplementary Section 1.2.

X-ray Diffraction. Grazing incidence X-ray diffraction (GIXRD) measurements were performed using the I07 beamline at Diamond Light Source in the UK (λ = 0.689 Å), using a vertical (2 + 2)-type diffractometer equipped with a Pilatus 100K area detector[58]. Membrane samples were cut into 1×2 cm^2 sized pieces and stuck onto glass supports, which were then mounted on a hexapod (PI-Micos) to allow independent alignment with 6 degrees of freedom during the data collections (Supplementary Fig. S49a). The measurements were conducted by moving the detector while maintaining a fixed sample position. The grazing incidence angle is set at 2°. Data collections were performed at room temperature using in-plane (over the 2θ range 3-40°, 0.50° step size) and out-of-plane (over the 2θ range 2-40°, 0.25° step size) measurement geometries and GIXRD scans were processed in DAWN 2[59]. GIXRD patterns were refined by Pawley refinement through TOPAS Academic[60]. High-resolution synchrotron powder X-ray diffraction (PXRD) data were collected using the I11 beamline at Diamond Light Source (λ = 0.827 Å). The full PXRD details are presented in the Supplementary Information.

For the *in situ* GIXRD measurements performed on solvated samples, pieces of Mylar film were used to cover the membrane surface with a thin layer of solvent (water, MeOH, acetone, and acetonitrile) during the GIXRD scans (Supplementary Fig. S49b). To investigate the reversible transformation between **CC3α**-PAN and **CC3γ'**-PAN, a membrane sample was removed from water without drying and covered with 1.0 mL of MeOH solvent layer before recording the GIXRD data (Supplementary Fig. S35). To more closely mimic the reversible membrane separation experiment where the feedstock was cycled between water and MeOH, a **CC3**-PAN sample was removed from water without drying, soaked in 100 mL MeOH for 1 minute, and covered with a thin layer of MeOH (1.0 mL) before the GIXRD measurement. The same process was repeated with the identical **CC3**-PAN sample using water or MeOH (Fig. 4e). For the *in situ* measurements performed using solvent vapours, nitrogen gas was bubbled through a 2L bottle that contained the organic solvent at a flow rate of 10 L·min^{-1}. The 'wet gas' generated during this process was then continually flowed over the membrane sample during the full measurement and Mylar film was used to seal the sample environment.

Separation Measurements. Solvent permeance and dye rejection measurements were performed using a Sterlitech® HP4750 dead-end membrane filtration system (Supplementary Fig. S22). We also used a commercial bench-scale 50 mL transparent Merck Millipore Amicon® dead-end stirred cell which is connected to an 800 mL Merck Millipore Amicon® RC800 reservoir to visualize the filtration process (Supplementary Fig. S23). During these measurements, the feedstocks were kept under a 10 bar nitrogen pressure (3 bar for Merck Millipore Amicon® cells) at room temperature, and the feedstock was continually stirred using a stirrer bar rotating at 400 rpm. Hansen solubility parameter (δ) and the physical properties of the organic solvents (Supplementary Table S2) were used to investigate the relationships between pure solvent permeances and the combined solvent properties.

Flux J (L·m^{-2}·h^{-1}) was calculated according to the following equation:

$$J = \Delta V / (A \times \Delta t) \qquad\qquad (Eq.1)$$

where ΔV is the volume of permeate collected in L in a given amount of time, A is the membrane surface area in m^2, and Δt is the time in hours between the start and end of the measurement.

Solvent permeance P (L·m^{-2}·h^{-1}·bar^{-1}) was calculated according to the following equation:

$$P = \Delta V / (A \times \Delta t \times p) \qquad\qquad (Eq.2)$$

where ΔV is the volume of permeate collected in L in a given amount of time, A is the membrane surface area in m^2, and Δt is the time in hours between the start and end of the measurement, p is the transmembrane pressure. To calculate solvent permeance, typically, 0.2 L of pure solvent or dye feedstock (20 ppm dye concentration) was added to the feedstock tank. The cell was then pressurised to 10 bar under nitrogen. The solvent permeate was then calculated based on the amount of time it took ~0.1 L of pure solvent or dye feedstock to flow through the membrane (see Supplementary Tables S3 and S4 for full details). The retentate was collected after each measurement. Error bars (*SD*) were calculated by the *STDEV.P* function using data obtained from at least three independent membranes.

For the dye rejection measurements, a series of dye feedstocks solutions in different solvents (water, MeOH, acetone, and acetonitrile) were prepared with a dye concentration of 20 ppm using the following dyes: reactive red 120 (RR, 1470 g·mol^{-1}), direct red 80 (DR, 1373 g·mol^{-1}), rose bengal (RB, 1018 g·mol^{-1}), brilliant blue (BB, 826 g·mol^{-1}), Congo red (CR, 697 g·mol^{-1}), protoporphyrin IX disodium (PPIX, 607 g·mol^{-1}), acid fuchsin (ACF, 585 g·mol^{-1}), sunset yellow (SY, 452 g·mol^{-1}), methyl orange (MO, 327 g·mol^{-1}), neutral red (NR, 289 g·mol^{-1}), and 4-nitrophenol (NP, 139 g·mol^{-1}) (see Supplementary Table S1 for full details). Ultraviolet-visible (UV-vis) spectroscopy was used to measure the dye concentration in the permeate to

calculate dye rejection performance. Dye rejection, R (%), of the membranes, was calculated as follows:

$$R = (1 - C_p / C_f) \times 100\% \qquad (Eq.3)$$

where C_p and C_f represent the dye concentrations in the permeate (C_p) and feed (C_f), respectively. Dye concentrations in permeate and feed were determined using a Cary 5000 UV-Vis-NIR spectrometer with the wavelengths specified in Supplementary Table S1. The MWCO was determined by interpolating from the plot of rejection against the molecular weight of the dyes and corresponds to the molecular weight for which rejection is 90%. During these measurements, the volume and the concentration of the permeate and the retentate were measured, and the mass balance of the feed solution could be calculated as follows:

$$C_f \times V_f = C_p \times V_p + C_r \times V_r \qquad (Eq.4)$$

where C_f, C_p, and C_r are the dye concentrations in ppm (g·L^{-1}) of the feed, permeate, and retentate, respectively; V_f, V_p, and V_r represent the volume of the feed, permeate, and retentate in L, respectively. Typically, 0.2 L of the feed solution was added into the cell, then 0.1 L permeate was collected, and 0.1 L retentate was left in the cell. Reversible filtration test, membrane absorption test, long-term operation, membrane stability test, water, and MeOH feedstock mixture separation experiments, graded sieving experiments for the ternary system are presented in Supplementary Section 1.4. The setup of a commercial bench-scale dead-end stirred filtration unit with transparent cells (a 50 mL transparent Merck Millipore Amicon® dead-end stirred cell connected to an 800 mL Merck Millipore Amicon® RC800 reservoir) is shown in Supplementary Fig. S23. Reversible filtration measurement data in water and MeOH is shown in Supplementary Table S5-S7, and dye rejection measurement data in water and MeOH mixture is shown in Supplementary Table S8.

Author contributions

A.I.C. and A.G.L. conceived the project. A.H. and Z.J. prepared the membranes. A.H. led the characterisation and membrane performance tests. Z.J. synthesised the PAN membrane support and conducted the AFM measurements. M.E.B. helped with the cage synthesis. H.H. and J.R. designed and set up the in-situ GIXRD system and helped with these measurements. A.H., M.A.L., and Y.W. contributed to the GIXRD measurements and processed the X-ray data. A.G.L. provided facility support and insights into advanced membrane science. Z.J. designed the interfacial synthesis method for the membrane. A.H. and M.A.L. conceived the graded molecular sieving part of the project and performed the associated measurements. M.A.L. co-supervised the project with A.I.C. and A.G.L. and wrote the manuscript with A.H. and Z.J. with contributions from all co-authors. All of the authors participated in the discussion of data and commented on the manuscript.

Competing interests

The authors declare no competing interests.

Data availability

The authors declare that the data supporting the findings of this study are available within the paper and its supplementary information file. Source data from chemical analysis, imaging, X-ray diffraction, liquid permeance, and separation measurements will be deposited in the Liverpool Elements repository (https://elements.liverpool.ac.uk/). Additional details can be obtained from the authors upon request.

References

1. Tozawa, T. *et al.* Porous organic cages. *Nat. Mater.* **8**, 973–978 (2009).
2. Zhang, G. & Mastalerz, M. Organic cage compounds – from shape-persistency to function. *Chem. Soc. Rev.* **43**, 1934–1947 (2014).
3. Jiang, S. *et al.* Molecular dynamics simulations of gas selectivity in amorphous porous molecular solids. *J. Am. Chem. Soc.* **135**, 17818–17830 (2013).
4. Giri, N. *et al.* Liquids with permanent porosity. *Nature* **527**, 216 (2015).
5. Sturluson, A., Huynh, M. T., York, A. H. P. & Simon, C. M. Eigencages: learning a latent space of porous cage molecules. *ACS Cent. Sci.* **4**, 1663–1676 (2018).
6. Jelfs, K. E. & Cooper, A. I. Molecular simulations to understand and to design porous organic molecules. *Curr. Opin. Solid State Mater. Sci.* **17**, 19–30 (2013).
7. Little, M. A. & Cooper, A. I. The chemistry of porous organic molecular materials. *Adv. Funct. Mater.* 1909842 (2020) doi:10.1002/adfm.201909842.
8. Chen, L. *et al.* Separation of rare gases and chiral molecules by selective binding in porous organic cages. *Nat Mater* **13**, 954–960 (2014).
9. Liu, M. *et al.* Barely porous organic cages for hydrogen isotope separation. *Science* **366**, 613–620 (2019).
10. Nunes, S. P. & Peinemann, K.-V. *Membrane technology: in the chemical industry*. (John Wiley & Sons, 2006).
11. Kim, D., Salazar, O. R. & Nunes, S. P. Membrane manufacture for peptide separation. *Green Chem.* **18**, 5151–5159 (2016).
12. Marchetti, P., Jimenez Solomon, M. F., Szekely, G. & Livingston, A. G. Molecular separation with organic solvent nanofiltration: A critical review. *Chemical Reviews* vol. 114 10735–10806 (2014).
13. Sholl, D. S. & Lively, R. P. Seven chemical separations to change the world. *Nat. News* **532**, 435 (2016).
14. Elimelech, M. & Phillip, W. A. The future of seawater desalination: Energy, technology, and the environment. *Science* vol. 333 712–717 (2011).
15. Kabay, N., Arda, M., Trochimczuk, A. & Streat, M. Removal of chromate by solvent impregnated resins (SIRs) stabilized by coating and chemical crosslinking. I. Batch-mode sorption studies. *React. Funct. Polym.* **59**, 9–14 (2004).
16. Jiang, Z., Karan, S. & Livingston, A. G. Water transport through ultrathin polyamide nanofilms used for reverse osmosis. *Adv. Mater.* **30**, 1705973 (2018).
17. Cundy, C. S. & Cox, P. A. The hydrothermal synthesis of zeolites: Precursors, intermediates and reaction mechanism. *Microporous Mesoporous Mater.* **82**, 1–78 (2005).
18. Thomas, A. Functional materials: from hard to soft porous frameworks. *Angew. Chemie Int. Ed.* **49**, 8328–8344 (2010).
19. Furukawa, H., Cordova, K. E., O'Keeffe, M. & Yaghi, O. M. The chemistry and applications of metal-organic frameworks. *Science* **341**, 1230444 (2013).
20. Côté, A. P. *et al.* Porous, crystalline, covalent organic frameworks. *Science* **310**, 1166–1170 (2005).
21. Lin, R.-B. *et al.* Multifunctional porous hydrogen-bonded organic framework materials. *Chem. Soc. Rev.* **48**, 1362–1389 (2019).
22. Dey, K. *et al.* Selective molecular separation by interfacially crystallized covalent organic framework thin films. *J. Am. Chem. Soc.* **139**, 13083–13091 (2017).
23. Matsumoto, M. *et al.* Lewis-acid-catalyzed interfacial polymerization of covalent organic framework films. *Chem* **4**, 308–317 (2018).
24. Corcos, A. R. *et al.* Reducing the pore size of covalent organic frameworks in thin-film composite membranes enhances solute rejection. *ACS Mater. Lett.* **1**, 440–446 (2019).
25. Zhang, C., Wu, B.-H., Ma, M.-Q., Wang, Z. & Xu, Z.-K. Ultrathin metal/covalent–organic framework membranes towards ultimate separation. *Chem. Soc. Rev.* **48**, 3811–3841 (2019).
26. Wang, Z., Zhang, S., Chen, Y., Zhang, Z. & Ma, S. Covalent organic frameworks for

separation applications. *Chem. Soc. Rev.* **49**, 708–735 (2020).

27. Venna, S. R. & Carreon, M. A. Metal organic framework membranes for carbon dioxide separation. *Chem. Eng. Sci.* **124**, 3–19 (2015).

28. Fenton, J. L., Burke, D. W., Qian, D., Cruz, M. O. de la & Dichtel, W. R. Polycrystalline covalent organic framework films act as adsorbents, not membranes. *J. Am. Chem. Soc.* **143**, 1466–1473 (2021).

29. Jones, J. T. A. *et al.* On-off porosity switching in a molecular organic solid. *Angew. Chemie Int. Ed.* **50**, 749–753 (2011).

30. Bera, S. *et al.* Porosity switching in polymorphic porous organic cages with exceptional chemical stability. *Angew. Chemie - Int. Ed.* **58**, 4243–4247 (2019).

31. Song, Q. *et al.* Porous organic cage thin films and molecular-sieving membranes. *Adv. Mater.* **28**, 2629–2637 (2016).

32. Brutschy, M., Schneider, M. W., Mastalerz, M. & Waldvogel, S. R. Porous organic cage compounds as highly potent affinity materials for sensing by quartz crystal microbalances. *Adv. Mater.* **24**, 6049–6052 (2012).

33. Bushell, A. F. *et al.* Nanoporous organic polymer/cage composite membranes. *Angew. Chemie Int. Ed.* **52**, 1253–1256 (2013).

34. Zhu, G., O'Nolan, D. & Lively, R. P. Molecularly mixed composite membranes: challenges and opportunities. *Chem. – A Eur. J.* **26**, 3464–3473 (2020).

35. Alexandre, P.-E. *et al.* A Robust Porous Quinoline Cage: Transformation of a [4+6] Salicylimine Cage by Povarov Cyclization. *Angew. Chemie Int. Ed.* **59**, 19675–19679 (2020).

36. Mastalerz, M., Schneider, M. W., Oppel, I. M. & Presly, O. A Salicylbisimine Cage Compound with High Surface Area and Selective CO2/CH4 Adsorption. *Angew. Chemie Int. Ed.* **50**, 1046–1051 (2011).

37. Avellaneda, A. *et al.* Kinetically Controlled Porosity in a Robust Organic Cage Material. *Angew. Chemie Int. Ed.* **52**, 3746–3749 (2013).

38. Ding, H. *et al.* Targeted synthesis of a large triazine-based [4+6] organic molecular cage: Structure, porosity and gas separation. *Chem. Commun.* **51**, 1976–1979 (2015).

39. Elbert, S. M. *et al.* Shape-Persistent Tetrahedral [4+6] Boronic Ester Cages with Different Degrees of Fluoride Substitution. *Chem. – A Eur. J.* **24**, 11438–11443 (2018).

40. Suganuma, S. & Katada, N. Innovation of catalytic technology for upgrading of crude oil in petroleum refinery. *Fuel Process. Technol.* **208**, 106518 (2020).

41. Jang, H.-Y. *et al.* Torlon® hollow fiber membranes for organic solvent reverse osmosis separation of complex aromatic hydrocarbon mixtures. *AIChE J.* **65**, e16757 (2019).

42. Lv, E., Ding, S., Lu, J., Yi, W. & Ding, J. Separation and purification of fatty acids by membrane technology: a critical review. *Int. J. Chem. React. Eng.* **18**, 20190224 (2020).

43. Gilmer, C. M., Zvokel, C., Vick, A. & Bowden, N. B. Separation of saturated fatty acids and fatty acid methyl esters with epoxy nanofiltration membranes. *RSC Adv.* **7**, 55626–55632 (2017).

44. Ghasemian, S., Sahari, M. A., Barzegar, M. & Gavlighi, H. A. Concentration of Omega-3 polyunsaturated fatty acids by polymeric membrane. *Int. J. Food Sci. Technol.* **50**, 2411–2418 (2015).

45. Takahashi, D., Inomata, T. & Fukui, T. AJIPHASE®: A Highly Efficient Synthetic Method for One-Pot Peptide Elongation in the Solution Phase by an Fmoc Strategy. *Angew. Chemie Int. Ed.* **129**, 7911–7915 (2017).

46. Thompson, K. A. *et al.* N-Aryl–linked spirocyclic polymers for membrane separations of complex hydrocarbon mixtures. *Science* **369**, 310–315 (2020).

47. Sadrzadeh, M. & Bhattacharjee, S. Rational design of phase inversion membranes by tailoring thermodynamics and kinetics of casting solution using polymer additives. *J. Memb. Sci.* **441**, 31–44 (2013).

48. Lu, Y., Chen, T., Chen, X., Qiu, M. & Fan, Y. Fabrication of TiO2-doped ZrO2 nanofiltration membranes by using a modified colloidal sol-gel process and its application in simulative radioactive effluent. *J. Memb. Sci.* **514**, 476–486 (2016).

49. Siew, W. E., Livingston, A. G., Ates, C. & Merschaert, A. Molecular separation with an

organic solvent nanofiltration cascade–augmenting membrane selectivity with process engineering. *Chem. Eng. Sci.* **90**, 299–310 (2013).

50. Little, M. A., Chong, S. Y., Schmidtmann, M., Hasell, T. & Cooper, A. I. Guest control of structure in porous organic cages. *Chem. Commun.* **50**, 9465–8 (2014).
51. Little, M. A. *et al.* Trapping virtual pores by crystal retro-engineering. *Nat. Chem.* **7**, 153–159 (2015).
52. Jones, J. T. A. *et al.* Modular and predictable assembly of porous organic molecular crystals. *Nature* **474**, 367 (2011).
53. Karan, S., Jiang, Z. & Livingston, A. G. Sub–10 nm polyamide nanofilms with ultrafast solvent transport for molecular separation. *Science* **348**, 1347–1351 (2015).
54. Aumann, L. & Morbidelli, M. A continuous multicolumn countercurrent solvent gradient purification (MCSGP) process. *Biotechnol. Bioeng.* **98**, 1043–1055 (2007).
55. Loftsson, T., Vogensen, S. B., Brewster, M. E. & Konráosdóttir, F. Effects of cyclodextrins on drug delivery through biological membranes. *Journal of Pharmaceutical Sciences* vol. 96 2532–2546 (2007).
56. Kohli, P., Wirtz, M. & Martin, C. R. Nanotube membrane based biosensors. *Electroanalysis* **16**, 9–18 (2004).
57. O'Brien, D. J. & Craig, J. C. Ethanol production in a continuous fermentation/membrane pervaporation system. *Appl. Microbiol. Biotechnol.* **44**, 699–704 (1996).
58. Nicklin, C., Arnold, T., Rawle, J. & Warne, A. Diamond beamline I07: A beamline for surface and interface diffraction. *J. Synchrotron Radiat.* **23**, 1245–1253 (2016).
59. Basham, M. *et al.* Data Analysis WorkbeNch (DAWN). **22**, 853–858 (2015).
60. TOPAS Academic version 4.1. *Coelho Software, Brisbane, Australia* (2007).